Large-scale epitaxy of two-dimensional van der Waals room-temperature ferromagnet Fe_5GeTe_2

Mário Ribeiro, Giulio Gentile, Alain Marty, Djordje Dosenovic, Hanako Okuno, Céline Vergnaud, Jean-François Jacquot, Denis Jalabert, Danilo Longo, Philippe Ohresser, et al.

npj | 2D Materials and Applications

www.nature.com/npj2dmaterials

ARTICLE OPEN

Check for updates

Large-scale epitaxy of two-dimensional van der Waals room-temperature ferromagnet Fe_5GeTe_2

Mário Ribeiro[1]✉, Giulio Gentile[1], Alain Marty[1], Djordje Dosenovic[2], Hanako Okuno[2], Céline Vergnaud[1], Jean-François Jacquot[3], Denis Jalabert[2], Danilo Longo[4], Philippe Ohresser[4], Ali Hallal[1], Mairbek Chshiev[1,5], Olivier Boulle[1], Frédéric Bonell[1]✉ and Matthieu Jamet[1]

In recent years, two-dimensional van der Waals materials have emerged as an important platform for the observation of long-range ferromagnetic order in atomically thin layers. Although heterostructures of such materials can be conceived to harness and couple a wide range of magneto-optical and magneto-electrical properties, technologically relevant applications require Curie temperatures at or above room temperature and the ability to grow films over large areas. Here we demonstrate the large-area growth of single-crystal ultrathin films of stoichiometric Fe_5GeTe_2 on an insulating substrate using molecular beam epitaxy. Magnetic measurements show the persistence of soft ferromagnetism up to room temperature in 12 nm-thick films, with a Curie temperature of 293 K, and a weak out-of-plane magnetocrystalline anisotropy. The ferromagnetic order is preserved in bilayer Fe_5GeTe_2, with Curie temperature decreasing to 229 K. Surface, chemical, and structural characterizations confirm the layer-by-layer growth, 5:1:2 Fe:Ge:Te stoichiometric elementary composition, and single-crystalline character of the films.

npj 2D Materials and Applications (2022)6:10 ; https://doi.org/10.1038/s41699-022-00285-w

INTRODUCTION

Until recently, long-range magnetic ordering was not thought possible in two-dimensional (2D) systems. The Mermin-Wagner theorem states that thermal fluctuations in a low-dimensionality isotropic Heisenberg model block the emergence of ferromagnetism (FM)[1]. In 2017, ferromagnetism was observed in exfoliated flakes of the 2D van der Waals (vdW) materials $Cr_2Ge_2Te_6$[2] and CrI_3[3]. These materials are electrical insulators, exhibit perpendicular magnetic anisotropy (PMA), and have Curie temperature (T_C) well below room temperature (RT). The prevailing understanding is that long-range ferromagnetic order in 2D vdW systems survives due to the spin-wave excitation gap opened by the strong intrinsic magnetocrystalline anisotropy (MCA). 2D vdW materials became a rich platform to explore low-dimensionality magnetism, and in a few years, the list of 2D vdW FMs increased with the addition of $FePS_3$[4], Fe_3GeTe_2[5], Fe_4GeTe_2[6], and $Fe_{5-\delta}GeTe_2$[7]. Fe-Ge-Te (FGT) ternary compounds in particular stood out due to their itinerant ferromagnetism, which is of great interest for spintronic applications.

Among the family of 2D vdW FMs, FGT compounds host a variety of noticeable magnetic effects, namely large anomalous- and planar topological Hall effect[8,9], magnetic skyrmions[10,11], Kondo lattices[12], and giant tunneling magnetoresistance[13]. To the best of our knowledge, the highest T_C in pristine, bulk vdW layered materials has been observed in $Fe_{5-\delta}GeTe_2$ and $CrTe_2$, with T_C~310 K[7,14,15]. Fe_3GeTe_2 exhibits a T_C of 230 K[16,17] in bulk form and 130 K[5] for a single layer. In these systems, the T_C can be tuned via the use of extrinsic mechanisms such as ionic gating[18], doping[19], ion implantation[20], proximity to topological insulators[21], and patterning methods[22]. Metastable states can be stabilized via temperature quenching and temperature cycles[23]. From a technological standpoint, high T_C is among the magnetic properties of highest interest for next-generation spintronic applications integrating 2D vdW FMs. $Fe_{5-\delta}GeTe_2$ is a Stoner-type itinerant ferromagnet, with asymmetric spin-up and spin-down density of states of the Fe 3*d* bands at the Fermi-level[24], spin-polarized metallic ligand bands[25], and near RT T_C. However, the mechanisms governing its magnetic properties are still unclear, with variable magnetic properties (T_C and anisotropy) being reported. Most experimental realizations have been done using Fe-deficient bulk crystals or micrometer-sized flakes exfoliated from them[7,23,26,27]. The properties of Fe_5GeTe_2 films with exact 5:1:2 stoichiometry remain unexplored. Recent studies pointed out the role played by Fe vacancies and the different Fe sublattices on the complex range of magnetic behaviors observed[6,7,23]. Additionally, magnetic critical exponents of bulk $Fe_{5-\delta}GeTe_2$ are close to those of a 3D Heisenberg and 3D XY systems[27], remaining unclear if these models still hold in ultrathin regimes.

While many of the demonstrations of vdW FMs materials relied on bulk crystals and on exfoliated flakes in the 2D limit, growth by molecular beam epitaxy (MBE) has been pursued to expand the complexity of the designed heterostructures and large-area scalability[21]. MBE is a well-established deposition technique for the realization of atomically thin single-crystal vdW materials and heterostructures with sharp interfaces[28]. Any outlook on future heterostructures and device concepts based on 2D vdW FMs requires the large-area fabrication of high-quality ultrathin films[28–32], for which MBE is well suited.

Here we demonstrate the MBE growth of single-crystal thin films of stoichiometric Fe_5GeTe_2 on an insulating substrate, Al_2O_3(001). In situ reflection high-energy electron diffraction (RHEED) measurements demonstrate the layer-by-layer growth of single-crystalline films. Chemical and structural characterization using Rutherford backscattering spectroscopy (RBS), scanning transmission electron microscopy (STEM), and X-ray diffraction (XRD), confirm the 5:1:2 Fe:Ge:Te stoichiometry and rhombohedral

[1]University Grenoble Alpes, CEA, CNRS, IRIG-Spintec, F-38000 Grenoble, France. [2]University Grenoble Alpes, CEA, IRIG-MEM, F-38000 Grenoble, France. [3]University Grenoble Alpes, CEA, IRIG-SYMMES, F-38000 Grenoble, France. [4]Synchrotron SOLEIL, L'Orme des Merisiers, 91192 Saint-Aubin, Gif-sur-Yvette, France. [5]Institut Universitaire de France (IUF), 75231 Paris, France. ✉email: mario.oliveiraribeiro@cea.fr; frederic.bonell@cea.fr

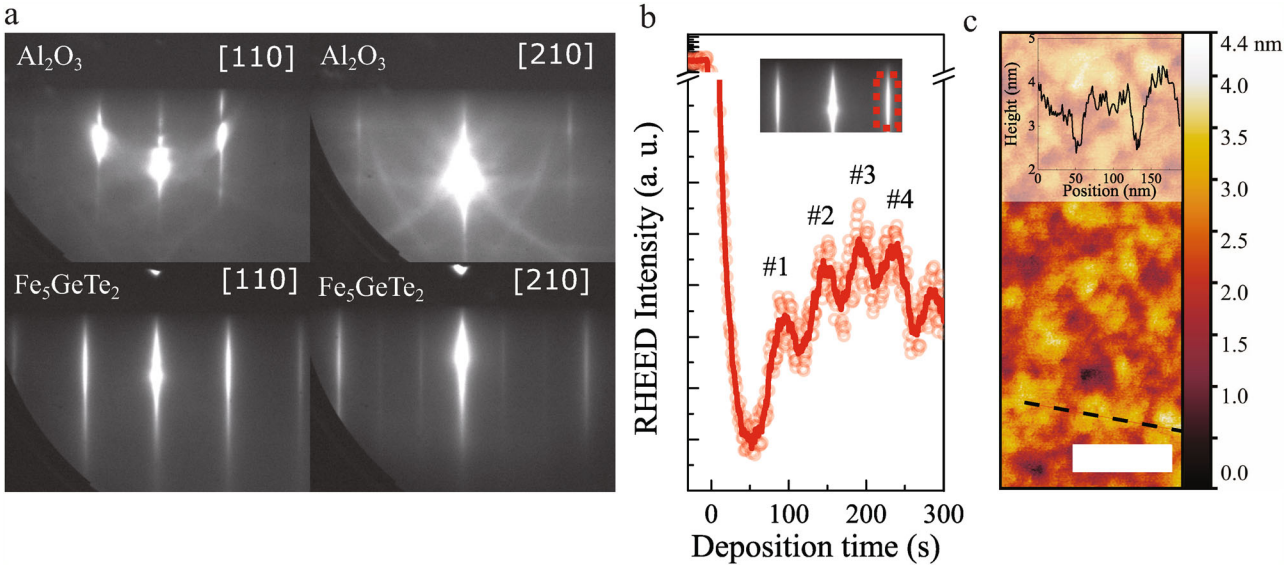

Fig. 1 Surface characterization of Fe_5GeTe_2. a RHEED patterns of the surface before and after the deposition of a 12 nm-thick film of Fe_5GeTe_2 along the [110] and [210] azimuths. **b** RHEED intensity oscillations of the (010) streak. The solid line is a moving average of the raw scatter data. Monolayer number identified on each oscilation. **c** Atomic force microscopy image of a 12 nm-thick film; scale bar 100 nm. Inset: Height profile showing resolved monolayer steps (1 ML ~ 0.977 nm).

crystal structure. Superconducting quantum interference device (SQUID), and X-ray magnetic circular dichroism measurements (XMCD) show a large magnetization saturation (M_S) of 644 kA m^{-1} at 10 K (1.95 μ_B/Fe), T_C of 293 K, and a magnetic critical exponent β of ~ 0.29 for 12 nm-thick films. Close to the 2D limit, bilayer Fe_5GeTe_2 retains the ferromagnetic order and critical exponent β ~ 0.29, and exhibits a lowering of the T_C and M_S to 230 K and 409 kA m^{-1} at 50 K (1.21 μ_B/Fe), respectively.

RESULTS

Structural and chemical characterization

The MBE growth of Fe_5GeTe_2 on Al_2O_3(001) was carried out in a home-built UHV deposition system with a base pressure in the low 10^{-10} mbar (see Methods for further information). Al_2O_3(001) is a conventional substrate used for epitaxy, electrically insulating, and has a hexagonal crystallographic structure. The substrates were first annealed in air at 1000 °C in a tube furnace to promote the formation of a terrace-and-step smooth surface, and again annealed in the UHV chamber at 800 °C for 20 min prior to the deposition. Ge and Te were co-deposited using Knudsen effusion and thermal cracker cells, respectively, and Fe using e-beam evaporation. The substrate temperature for the growth of Fe_5GeTe_2 was set to 350 °C, the flux ratio of Fe:Ge was kept to the stoichiometric 5:1, and the Te flux on overpressure (approximately twice the stoichiometric flux). After the deposition, the films were annealed for 20 min at 550 °C under Te flux, and then capped with a 3 nm-thick Al film at RT. The growth of Fe_5GeTe_2 on Al_2O_3(001) was monitored in situ using RHEED. We report mainly on the characterization of 12 nm-thick Fe_5GeTe_2 films (1 monolayer (ML) ~0.977 nm). In Fig. 1a, the top left side panel shows well-defined RHEED patterns of the Al_2O_3(001) surface with the electron-beam (e-beam) aligned along [110], while the bottom left panel shows the diffraction pattern for the same direction after the growth of 12 nm of Fe_5GeTe_2. Similarly, the top and bottom right-side panels show the diffraction patterns of the Al_2O_3(001) surface before and after the growth of 12 Fe_5GeTe_2 layers, respectively, with the e-beam aligned along [210] (see Supplementary Fig. 1 for RHEED snapshots during the deposition and annealing of 12 and 2 nm-thick samples).

Despite the large lattice misfit with Al_2O_3(001) (~−15 %), the sharp streaks and anisotropic RHEED patterns demonstrate the single-crystalline character of Fe_5GeTe_2, with *c*-axis perpendicular to the surface. The two azimuths are aligned with those of the Al_2O_3(001) surface, showing the Al_2O_3(001)[100]/Fe_5GeTe_2(001)[100] epitaxial relationship. The real-time monitoring of the RHEED intensity of the 1st order diffraction streaks allowed for the observation of periodical intensity oscillations characteristic of a layer-by-layer growth mode (Fig. 1b). By indexing the successive oscillations as the formation of a single layer, the rate of growth was estimated at 1.69 monolayers per minute of deposition. Atomic force microscopy (AFM) scans of the surface of 12 nm-thick films not capped with Al, taken within minutes of exposing the surface to the environment, show a smooth surface with root-mean-square roughness (RMS) of 0.5 nm, without clearly defined terraces, but with atomic steps corresponding to those of one or multiple monolayers (Fig. 1c).

To gather further information on the crystallographic structure, domain size, mosaic spread, and lattice parameter distribution of the films deposited, we performed in-plane (grazing incidence) and out-of-plane XRD measurements (see Methods for further details). Fe_5GeTe_2 is a highly anisotropic layered vdW ferromagnet with a trigonal crystal system. Typical lattice constants reported in the literature for bulk $Fe_{5-\delta}GeTe_2$ are $a \approx 4.04$ Å and $c \approx 29.19$ Å[7,23,33]. Unit cells are typically represented with three stacked Fe_5GeTe_2 layers, with vdW gaps between adjacent Te planes. The complex atomic arrangement, the common presence of stacking faults and vacancy-induced disorder makes the precise determination of the crystallographic structure an open issue[7,23,26,33]. In Fig. 2a, we depict the unit cell and three Fe_5GeTe_2 layers viewed along the [100] direction, according to the crystallographic model of ref. [7]. The model considers Fe deficiency via fractional occupation probabilities of the Fe sites, and includes a split Ge and Fe1 site with half-occupation probability. Figure 2b shows the out-of-plane $\theta/2\theta$ diffraction scan of a 12 nm-thick film, where we index the Al_2O_3(00 *l*) and Fe_5GeTe_2(00 *l*) Bragg peaks. The determined unit cell lattice constant $c \approx 29.3$ Å is in good agreement with previous reports (thickness of 1 ML = c/3)[7,23,33]. The fringes around the Bragg peaks of Fe_5GeTe_2(009) indicate low surface and interface roughness (also confirmed by the RMS of 0.5 nm measured by AFM in Fig. 1c), and allows for the estimation

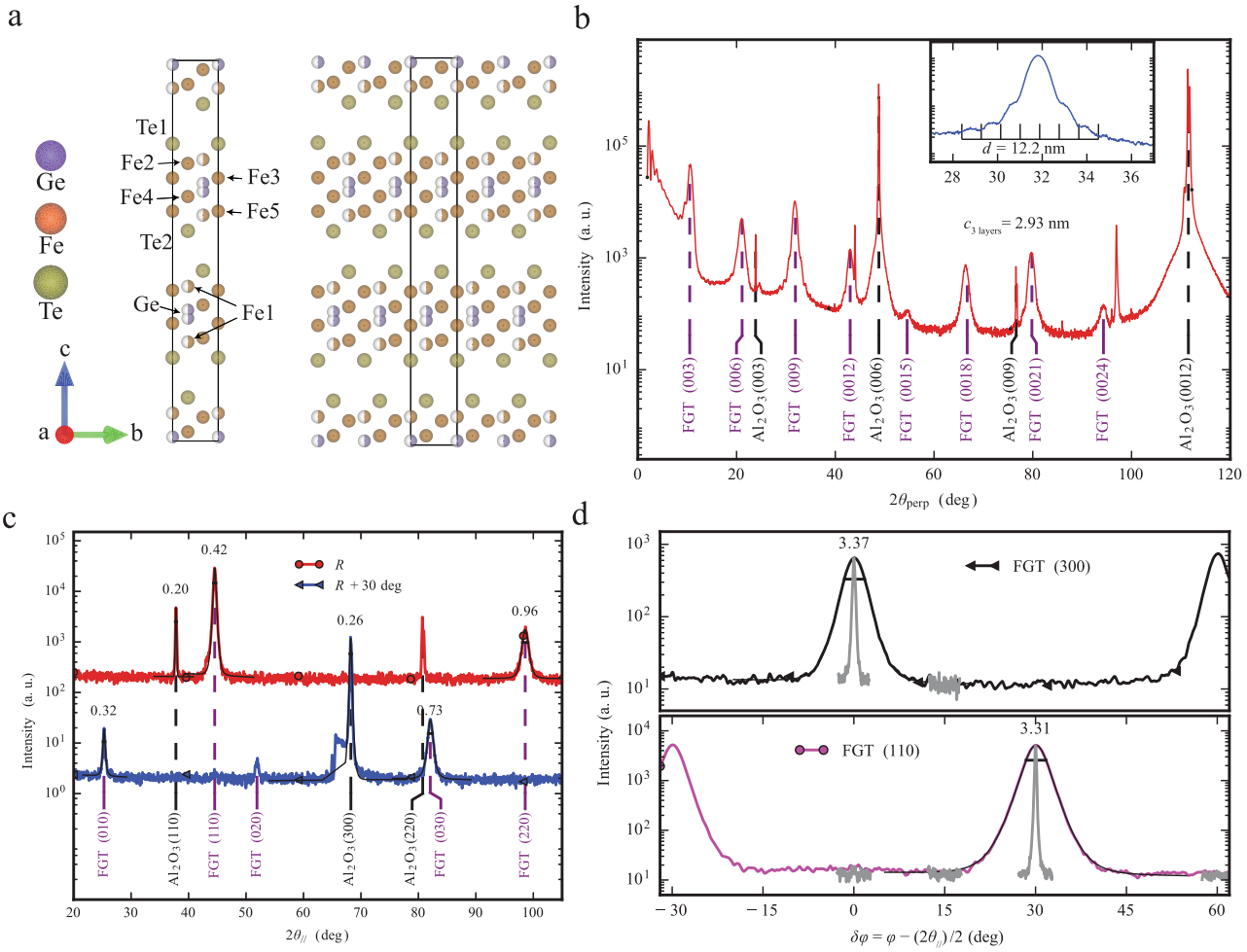

Fig. 2 Structural characterization of Fe_5GeTe_2 by X-ray diffraction. a Unit cell projected along [100], with FGT layers separated by the vdW gap between adjacent Te sublayers. The right-side image shows the same projection for several repetitions of the unit cell. The occupation probability is represented by half-filled solid balls. Images generated using VESTA software[52] for the crystallographic model of ref. [7]. **b** Out-of-plane $\theta/2\theta$ XRD scan of the films, showing $Al_2O_3(00\,l)$ and Fe_5GeTe_2 $(00\,l)$ peaks. Inset: zoom on the (009) Bragg peak to show the fringes used to estimate the film thickness. **c** In-plane radial XRD scans along the (110) reciprocal direction (*R*), and (010), (*R*+30°). Each diffraction peak is labelled with the full widh at half maximum. **d** In-plane azimuthal XRD scan over the families {110} and {300} showing the 6-fold symmetry of the crystal. Gray lines show the corresponding radial peak.

of a film thickness of 12.5 ± 0.3 nm, in strong agreement with the expected growth of 12 layers determined from the RHEED oscillations (See Supplementary Fig. 2 for the XRD analysis of a 2 nm-thick film). In Fig. 2c, we show in-plane radial scans $\theta_{//}/2\theta_{//}$ that were acquired along the (*hh*0) and (0*h*0) reciprocal directions, 30° apart from each other. The full width at half maximum (FWHM) is also displayed above the peaks. From these scans, we obtain an in-plane lattice parameter $a = 4.068$ Å, expanded by roughly 0.7% compared to the reference value of 4.04 Å. The mutually exclusive presence of the (*hh*0) and (0*h*0) peaks on each radial scan indicate the absence of domains rotated by at least 30°. This is further confirmed in Fig. 2d, which shows the azimuthal dependence of the intensity of the Bragg peaks identified in the radial scans (grey curves). The baseline of the azimuthal scans is the sum of the instrumental background and of the signal from misaligned crystallites with an isotropic distribution of orientations. The observed correspondence between the azimuthal and radial baselines implies that there is no isotropic component in the crystallites angular distribution. The film is single crystalline with the expected 60° periodicity of the basal plane of the crystal lattice. Noticeably, the FWHM for the Bragg peaks is substantially larger. From the study of the momentum transfer for each radial and azimuthal Bragg diffraction peak and its dispersion, one can estimate the domain size *D*, lattice parameter distribution $\Delta a/a$, and in-plane mosaic spread $\Delta\xi$ of the film[34,35] (see Supplementary Note 1 and Supplementary Fig. 3 for details on the calculations). For the 12 nm-thick film, *D* was determined to be 33 nm, which must be considered as a lower bound for the domain size due to the instrumental limited resolution, $\Delta a/a \approx 0.66$ %, and $\Delta\xi \approx 3.34$ °, values that corroborate the single-crystalline character of the deposited films.

In order to take a closer look at the disorder and stacking of the Fe_5GeTe_2 ultrathin films, we recorded atomic-resolution real-space images by STEM (see Methods for further information). Figure 3a shows a high-angle annular dark-field (HAADF) cross-section image along [100]. The atomically flat Al_2O_3 promoted the epitaxy of well-oriented layers that are uniform over large areas, parallel to each other, and with no perceivable rotated domains. At the interface between the two materials, there is a thin amorphized gap of 6 Å, after which the first Fe_5GeTe_2 layer develops. The lattice parameters determined from Fourier transform analysis of the HAADF image, $a = 4.07 \pm 0.02$ Å and $c = 29.4 \pm 0.3$ Å, are in strong agreement with the ones obtained from XRD.

Chemical analysis using RBS spectroscopy confirms the nominal 5:1:2 stoichiometry of the Fe:Ge:Te elementary composition of the film (inset of Fig. 3a). Energy-dispersive X-ray spectroscopy (EDX)

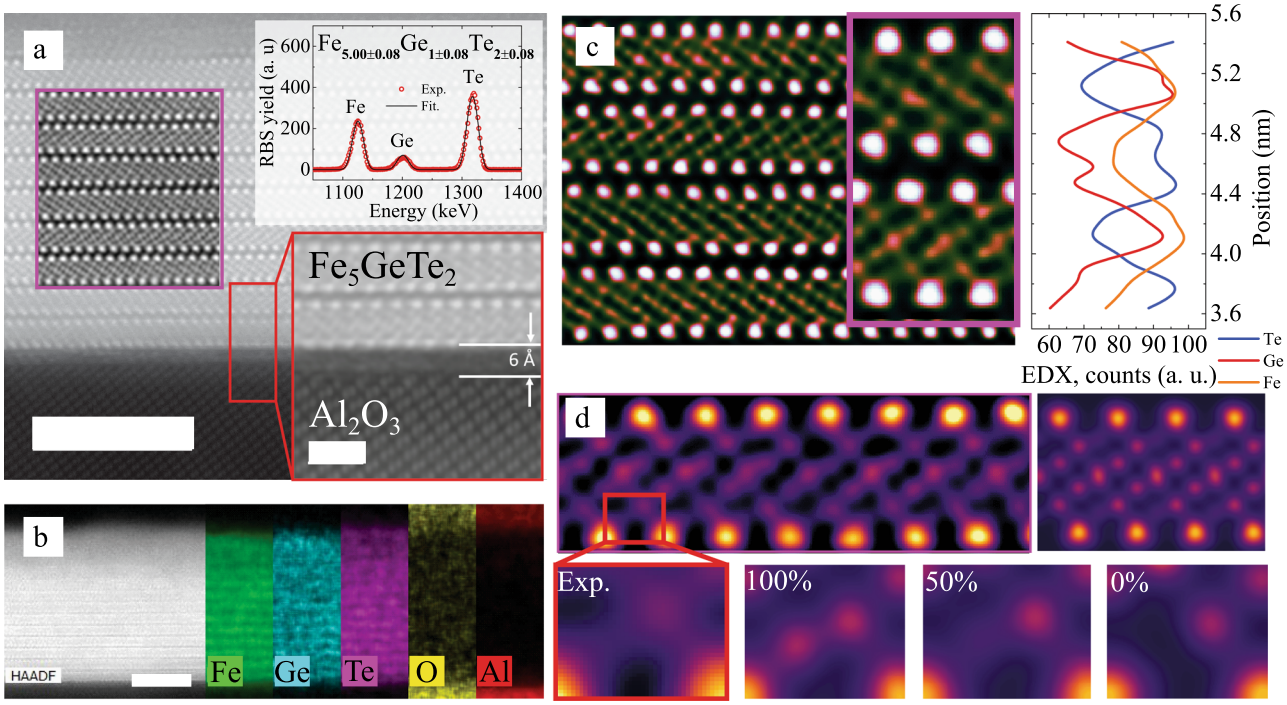

Fig. 3 Transmission electron microscopy of Fe_5GeTe_2. a High-angle annular dark-field (HAADF) cross-section image of the 12 nm-thick film along [100]. Left scale bar, 5 nm. Left inset: High-pass filtered image of the layers. Top inset: Rutherford backscattering spectroscopy showing stoichiometric 5:1:2 Fe:Ge:Te composition. Bottom inset: Zoomed view of the interface between Al_2O_3 and Fe_5GeTe_2; scale bar 1 nm. **b** Element distribution across the layers, determined using energy-dispersive X-ray spectroscopy (EDX); scale bar 5 nm. **c** Atomic number contrast-enhanced HAADF image of the Fe_5GeTe_2 layers. The right plot shows an EDX scan over two layers, selective to Te, Ge, and Fe. **d** Comparison between experimental (top left) and simulated (top right) *Z*-constrast-enhanced HAADF images. Bottom images are zooms on the Fe1 site. The simulations consider different occupation probabilities of the Fe1 site.

shows a homogenous distribution of each element in the film (Fig. 3b). In Fig. 3c, *Z*-contrast-enhanced HAADF over a smaller section of the film yields a site distribution with a clear indication of the presence of heavier atoms at the edges of the layers. Element resolved EDX over two layers shows the clear presence of Fe and Ge in between Te sites. Fe shows a broader dependence on position than Ge, as expected from its distribution in the cell. The presence of the Fe1 atom is not clearly resolved in our measurements, but the symmetry of the images points to a 50 % occupation probability in the two possible sites, as in the model of ref. [26]. In order to confirm it, we performed simulations of *Z*-contrast HAADF images for several occupation probabilities (Fig. 3d). For a 100 % occupation probability, the simulation indicates that an STEM scan should be able to clearly resolve the site occupied by the Fe1 atom, while at 0 % the background strongly contrasts with the atomic sites. At 50 %, we observe a tail connecting the inner Fe2 atoms to Te. This reproduces well the experimental result, and strongly suggests that a crystallographic model with a Fe1 half-split site applies to our epitaxial films.

Characterization of the magnetic properties

The magnetic properties of the films were characterized using SQUID and XMCD (see Methods for further information). In Fig. 4a and Fig. 4b we plot isothermal magnetic hysteresis loops at different temperatures with the magnetic field applied in the *ab* basal plane, and along the *c*-axis of the layers, respectively, for 12 nm-thick films (12 ML). The data have been corrected by subtracting the magnetic background observed at temperatures well above T_C, and a residual slope due to a paramagnetic contribution from the substrate below 50 K. The same slope was subtracted from the in-plane and out-of-plane field dependences. The subtraction of the magnetic background signal was justified from the comparative study of the XMCD and SQUID measurements, in which the latter had a systematic shift equivalent in magnitude to the parasitic magnetic background observed above T_C, indicating that the SQUID was capturing a signal not related to the film. The insets show the raw magnetization curves and the considered background in gray. The in-plane hysteresis loops show low coercivity (~ 4 mT at 50 K) and saturation field (~ 200 mT at 50 K) (see Supplementary Fig. 4 for a zoom-in over a narrower field range of the in-plane magnetic hysteresis loops). The saturation magnetization averaged over in-plane and out-of-plane measurements amount to $M_S = (644 \pm 54)$ kA m^{-1} at 10 K, corresponding to a magnetic moment $m = (1.95 \pm 0.12)$ μ_B/Fe. These values are in-line with those previously reported for Fe-deficient $Fe_{5-\delta}GeTe_2$ ($\delta = 0.1$–0.3) films exfoliated from bulk crystals[23,25]. Perpendicular to the surface, the saturation field largely increases, indicating an easy-plane magnetic anisotropy. We confirmed the consistency of the SQUID magnetic field dependences with polar magneto-optical Kerr effect and XMCD field dependences (see Supplementary Fig. 5).

In Fig. 4c, the temperature dependence of the remanent magnetization (M_r) closely follows the scaling behavior of an ordered ferromagnetic system, $M_r \propto \left(\frac{T_C - T}{T_C}\right)^{\beta}$, yielding $T_C = (292.6 \pm 2.6)$ K and $\beta = 0.29 \pm 0.05$. This behavior is in striking contrast to the complex temperature dependences observed in bulk and Fe-deficient $Fe_{5-\delta}GeTe_2$ films[7,23], suggesting that MBE-grown films present a higher structural and chemical homogeneity. The M_r can be reasonably fitted with 3D models (see Supplementary Fig. 6). Our determined β significantly deviates from the one observed in bulk crystals $\beta \approx 0.346$[27]. While the reduction in the magnitude of β might point towards an approach to the window of magnetic critical exponents of 2D systems, the analysis of the residuals of the fittings to different magnetic critical exponent models suggests that a 3D model is better suited to

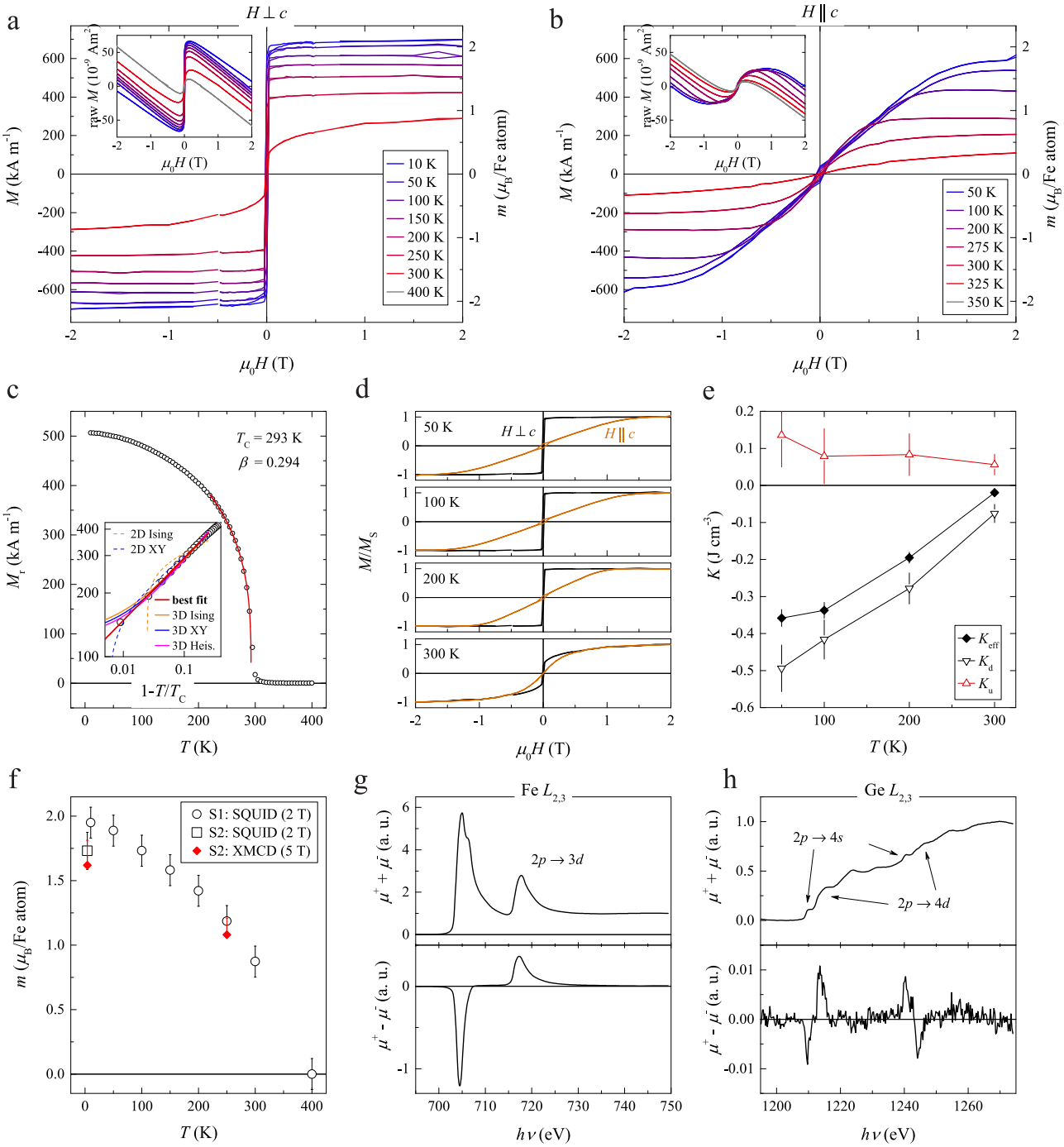

Fig. 4 Magnetic characterization of 12 nm-thick Fe_5GeTe_2 using SQUID and XMCD. a Isothermal magnetic hysteresis loops with the external magnetic field H in the *ab* basal plane for different temperatures. The magnetic background at temperatures well above T_C has been subtracted for all measurements. Inset: Raw data highlighting the magnetic background considered. **b** Same as **a**, with H parallel to the *c*-axis. **c** Remanent magnetization as a function of temperature. Fitting to the scaling behavior of a magnetic system in an ordered state yields $T_C \approx 293$ K and $\beta \approx 0.294$. The inset shows the scaling behavior of the remanence for different 2D and 3D magnetic critical exponents (see Supplementary Fig. 6). **d** Normalized in-plane and out-of-plane magnetic hysteresis loops for different temperatures. **e** Effective magnetic anisotropy, K_{eff}, shape anisotropy, K_d, and uniaxial anisotropy, K_u, as a function of temperature. **f** Magnetic moment per Fe atom as a function of temperature determined from SQUID and XMCD for two 12 nm-thick samples (S1 and S2). **g** Normalized Fe $L_{2,3}$-edge X-ray absorption spectroscopy (XAS) ($\mu^+ + \mu^-$) and XMCD ($\mu^+ - \mu^-$) spectra. $\mu^{+(-)}$ is the absorption for parallel (antiparallel) alignment of the light helicity and the sample magnetization. **h** Normalized Ge $L_{2,3}$-edge XAS and XMCD.

describe the magnetic behavior of the films (Supplementary Fig. 6). Figure 4d shows the normalized in-plane and out-of-plane isothermal magnetic loops at 50, 100, 200, and 300 K. We determine the effective anisotropy K_{eff} from the area enclosed between the curves. The uniaxial anisotropy K_u is deduced from K_{eff} and the measured M_S, with the relation $K_{eff} = K_u + K_d = K_u - (\mu_0/2)M_S^2$, where K_d is the shape anisotropy and μ_0 the vacuum permeability. The temperature dependence of K_{eff}, K_u,

and K_d is displayed in Fig. 4e. We estimate a small positive uniaxial anisotropy $K_u \approx 0.09$ J cm^{-3} that favors an easy *c*-axis, but remains weaker than shape anisotropy at all temperatures. Figure 4f shows the magnetic moments of this sample (S1) determined by SQUID and compares it to the magnetic moment of a second sample (S2) measured by both SQUID and XMCD. Sample S2 was capped with 5 nm of Te instead of Al. For sample S2, the excellent agreement between SQUID and XMCD confirms the validity of the background correction of SQUID measurements. The smaller magnetic moment of sample S2 compared to that of sample S1 (whose 5:1:2 Fe:Ge:Te composition was ascertained by RBS, in Fig. 3a) might originate from Fe deficiency. In Fig. 4g,h we detail the XMCD characterization of sample S2, and show the XMCD spectra at the Fe and Ge $L_{2,3}$ edges at 4 K (see Methods for further details). The measurements were performed in total electron yield mode, with X-ray incidence normal to the surface ($\alpha = 90°$), and the ±5 T magnetic field parallel to the beam direction. Additional measurements were carried out at $\alpha = 30°$ (not shown). We applied the conventional sum rules analysis[36,37] to the Fe absorption signal in order to determine the effective spin ($m_S^{\mathrm{eff},\alpha} = m_S + m_D^{\alpha}$) and orbital ($m_L^{\alpha}$) moments (see Supplementary Note 2 for further details on the determination of the Fe magnetic moments with XMCD sum rules). From those, we derive the isotropic spin (m_S) and orbital (m_L) moments, as well as the intra-atomic dipole moment anisotropy $\Delta m_D = m_D^{\perp} - m_D^{\parallel}$ and the orbital moment anisotropy $\Delta m_L = m_L^{\perp} - m_L^{\parallel}$ ($\perp$ and $\parallel$ denote the out-of-plane and in-plane components, respectively). We obtained $m_S = 1.54$ μ_B, $m_L = 0.08$ μ_B, $\Delta m_D = 0.21$ μ_B, and $\Delta m_L = -0.01$ μ_B. The total magnetic moment amounts to $m_S + m_L = 1.62$ μ_B, in excellent agreement with the theoretical value determined from the first principles reported in Table 1 (see Methods for further details).

The small m_L and Δm_L are consistent with the weak out-of-plane uniaxial magnetic anisotropy deduced by SQUID measurements. We also observed a small polarization of Ge atoms, in agreement with ref. [25]. and with our ab initio results (Table 1). As depicted in Fig. 4h, both $2p \rightarrow 4d$ ($\Delta L = +1$) and $2p \rightarrow 4s$ ($\Delta L = -1$) transitions present a finite XMCD signal. The sign of the XMCD for 4*d* (4*s*) final states is equal (opposite) to the one of Fe. Given the opposite sign of ΔL for these transitions, we deduce that the magnetic moment of both 4*d* and 4*s* bands is opposite to the Fe one. In ref. [25], a sizeable magnetic moment was also observed on Te atoms, but we could not confirm it in our film due to the use of a Te capping layer. Note that we neglected the Ge and Te contributions to determine the Fe magnetic moment by SQUID. According to Table 1, these assumptions lead to an underestimation of the Fe magnetic moment by only 2%.

Table 1. Estimated magnetic moments of Fe_5GeTe_2.

Atom	m_S (μ_B/at.)	m_L (μ_B/at.)	$m_S + m_L$ (μ_B/at.)
Te1	0.00	0.00	0.00
Fe1	−0.16	−0.03	−0.19
Fe2	2.35	0.05	2.40
Fe3	2.10	0.04	2.14
Ge	−0.06	0.00	−0.06
Fe4	1.50	0.03	1.53
Fe5	2.60	0.08	2.68
Te2	−0.10	−0.02	−0.12
Fe (averaged)	1.68	0.03	1.71
Fe (exp.)	1.54	0.08	1.62

Spin (m_S), orbital (m_L), and total ($m_S + m_L$) magnetic moment per atom in Fe_5GeTe_2, estimated from first principles calculations. A single Fe1 site was considered to have 100% occupancy (see text). The last two lines give the calculated averaged Fe magnetic moments and the experimental values measured by XMCD, respectively.

Figure 5 shows the magnetic properties of 2 nm-thick films (2 ML of Fe_5GeTe_2) measured by SQUID. Figure 5a and Fig. 5b show isothermal magnetic hysteresis loops at different temperatures with the external magnetic field applied in the *ab* basal plane, and along the *c*-axis of the layers, respectively. Compared to the 12 nm-thick films, M_S decreases by roughly 40%, with $M_S = (409 \pm 5)$ kA m^{-1} at 10 K (averaged over in-plane and out-of-plane measurements), corresponding to a magnetic moment $m = (1.21 \pm 0.01)$ μ_B/Fe. In Fig. 5c we plot the temperature dependence of M_r and fit the results to $M_r \propto \left(\frac{T_C - T}{T_C}\right)^{\beta}$. The fitting yields $T_C = (229.4 \pm 0.3)$ K and $\beta = 0.29 \pm 0.01$.

DISCUSSION

The magnetic properties of the films (M_S, K_u, and T_C) are in good general agreement with those reported for bulk crystals synthesized using chemical vapor transport (CVT). Nonetheless, some differences are noticed. More complex magnetic properties were reported in CVT $Fe_{5-\delta}GeTe_2$, which are not observed in our MBE-grown films. In particular, we do not observe PMA nor anomalies in the temperature dependence of M_r.

Weak PMA has been reported in mono to few-layer flakes[7,38,39], while bulk crystals show in-plane magnetic anisotropy[27,40–42] or no magnetic anisotropy[23]. When shape anisotropy is taken into account, all reports so far agree on the presence of a weak uniaxial anisotropy. We confirm the weak uniaxial anisotropy, but in our films it never overcomes shape anisotropy. It is possible that both K_u and M_S are affected by the 2% larger volume of the unit cell in our crystals ($a = 4.07$ Å, $c = 29.30$ Å) when compared to those of works reporting PMA ($a \sim 4.04$ Å, $c \sim 29.1 - 29.2$ Å)[7,38,39]. Fe deficiency might also play a role. It is likewise possible that AlO_x and Te capping layers induce a negative interface anisotropy that reduces the overall K_u.

Concerning the temperature dependence of M_r, complex variations have been reported for CVT crystals[7,23]. Quenched crystals produced by this method stabilize metastable states with higher T_C and exhibit a first-order phase transition at $T \sim 110$ K originating from irreversible changes in the crystalline structure[7,23,26]. In our case, it appears that the different growth method and thermal history prevents the formation of such metastable states. An additional anomaly around 100 K has been related to the ordering temperature and fluctuations of the Fe1 magnetic moments that are possibly sensitive to the Fe deficiency[7,26]. An alternative interpretation involved the formation of "glassy clusters"[40], which are unlikely in our layers given the high crystalline quality. Since the body of literature points towards a high sensitivity of the magnetic properties on local inhomogeneities, we believe that the anomalies are of extrinsic origin and connected to the non-uniformity and disorder of the films. We speculate that our films simply do not show such complex behavior because of the higher homogeneity, uniformity and negligible Fe deficiency, as supported by our comprehensive characterization.

A striking result is the apparent 3D magnetic behavior of the films, even in the 2D limit. The $\beta \sim 0.29$ exponent hardly varies with the thickness (12 ML and 2 ML) and the T_C remains surprisingly large (229 K) in bilayers. This may be related to the atomic coordination of Fe_5GeTe_2. Actually, a monolayer is composed of 6 atomic slabs of Fe stacked onto each other (4 fully occupied layers + 2 layers with 50% occupation). On top of that, the Te terminations also mediate the ferromagnetism in the system[25]. Therefore, in contrast to 2D ferromagnets like CrI_3, where all magnetic atoms lie in the same plane, Fe_5GeTe_2 contains a 3D-like network of magnetic elements. This atomic configuration

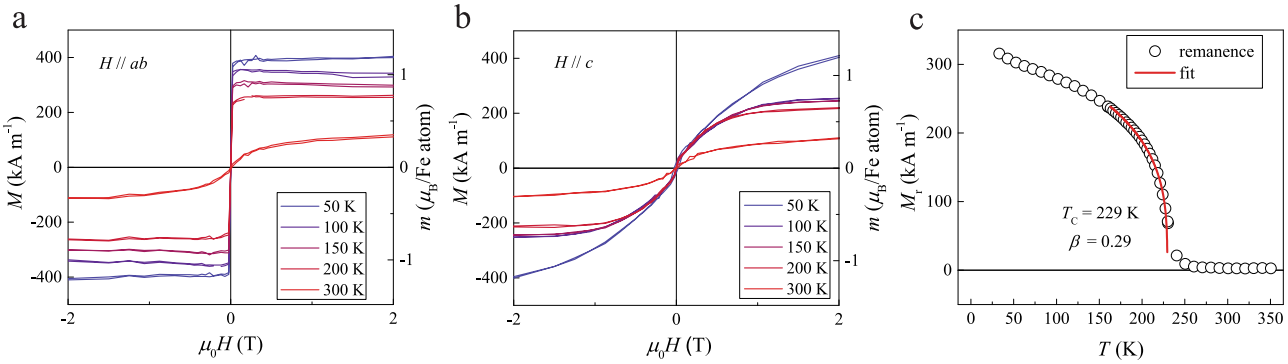

Fig. 5 Magnetic characterization of 2 nm-thick Fe_5GeTe_2. a Isothermal magnetic hysteresis loops with the external magnetic field *H* in the *ab* basal plane for different temperatures. **b** Same as **a**, with external magnetic field *H* parallel to the *c*-axis. **c** Remanent magnetization as a function of temperature. Fitting to the scaling behavior of a magnetic system in an ordered state yields $T_C \approx 229$ K and $\beta \approx 0.29$. (see Supplementary Fig. 6 for a comparison with different 3D and 2D magnetic critical exponents).

implies a 3D-like exchange interaction, which results in the observed 3D magnetic behavior. This corroborates the idea developed in Ref. [6]. that the large number of spin-pairs in Fe_5GeTe_2 enhances the exchange interaction and results in a large T_C in spite of the weak magnetocrystalline anisotropy. The weak thickness dependences of T_C and β therefore point to sizable intralayer out-of-plane exchange interactions and suggest comparatively weak interlayer interactions, in consistency with the layered nature of Fe_5GeTe_2. Concerning the exact critical behavior of Fe_5GeTe_2 thin films, a further study of the γ and δ critical exponents would be needed to unambiguously characterize the magnetic interactions.

In summary, we demonstrated the large-scale growth of few-layer, single-crystal Fe_5GeTe_2 on Al_2O_3(001) using molecular beam epitaxy, and provided a thorough structural and magnetic characterization. We showed that the MBE technique yields Fe_5GeTe_2 layers with high structural quality, layer-by-layer growth, virtually no Fe deficiency, and room-temperature ferromagnetism. STEM images and simulations clearly indicate a crystallographic structure with half-split occupation probability of the Fe1 atomic site. The 12 ML ultrathin films exhibit soft ferromagnetism, a large magnetization of about 644 kA m^{-1} at 10 K, easy-plane magnetization, with a weak *c*-axis magnetocrystalline anisotropy $K_u \sim 0.09$ J cm^{-3}. Bilayer Fe_5GeTe_2 retains the ferromagnetic order, with a lower magnetization of 409 kA m^{-1} at 10 K, and a significant T_C of 229 K. Analysis of the β critical exponent indicates a thickness-independent 3D magnetic behavior, attributed to the 3D-like coordination between Fe sublattices inside vdW monolayers, and responsible for the high T_C.

Our work highlights the role of MBE as a key tool for the fine tailoring of 2D vdW FMs single crystals. In the particular case of Fe_5GeTe_2, we have grown a benchmark material with exact stoichiometry and well-defined crystalline structure to well-establish the magnetic properties of this vdW ferromagnetic material. It will serve as a platform to further unveil the complex dependence of the magnetic properties on the film composition and crystal structure, and as a stepping stone towards the integration in large-scale vdW multilayers for spintronics.

METHODS

MBE

1×1 cm^2 Al_2O_3(001) substrates were cleaned prior to the tube furnace annealing with a standard isopropanol/acetone ultrasonic bath. For the growth of Fe_5GeTe_2, high-purity Ge (99.999%) was evaporated at 1060 °C, while high-purity Te (99.999%) was evaporated at 330 °C and cracked at 1000 °C. Fe (99.99%) was evaporated following standard e-beam procedures. Fe and Te deposition rates were calibrated by AFM on pre-patterned samples. The Ge deposition rate was calibrated with homoepitaxial RHEED oscillations on Ge(111). The Fe flux rate was monitored during the deposition using a quartz microbalance, while the Ge and Te flux rates were monitored before and after the depositions with a UHV pressure gauge.

XRD

In-plane XRD measurements were performed with a SmartLab Rigaku diffractometer operating at 45 kV and 200 mA. Collimators with a resolution of 0.5° were used both in the source and the detector. The measurements were done with a copper rotating anode beam tube ($K_\alpha =$ 1.54 Å) at a grazing incident angle of 0.4°. The out-of-plane XRD measurements were performed using a Panalytical Empyrean diffractometer operated at 35 kV and 50 mA, with a cobalt source, ($K_\alpha = 1.79$ Å). A PIXcel-3D detector allowed a resolution of 0.02° per pixel, in combination with a divergence slit of 0.125°.

AFM

The film topography was characterized with a Bruker Dimension-Icon microscope using a scanasyst-air cantilever, operated in ScanAsyst mode, and under ambient conditions. The root-mean-square roughness was evaluated on 1×1 μm^2 areas.

STEM

STEM measurements were performed using a Cs-corrected FEI Themis at 200 keV. HAADF-STEM images were acquired using a convergence semi-angle of 20 mrad and collecting scattering from >60 mrad. EDX was performed for elemental mapping using a Bruker EDX system consisting of four silicon drift detectors in the Themis microscope. STEM specimens were prepared by the focused ion-beam lift-out technique using a Zeiss DualBeam Cross Beam uSTE750 at 30 kV.

HAADF-STEM simulations were carried out using multislice simulation software, namely JEMS[43], and μSTEM[44] including the experimental conditions used for the image acquisition. The model structures were constructed based on the crystal information given in refs. [26,33].

RBS

Rutherford backscattering was done using an ion-beam of $^4He^+$ ions with 2 MeV, at a chamber pressure of 10^{-6} mbar, with a 160° angle between the incident beam and the detector, and an angle of incidence of 75°.

SQUID

SQUID measurements were performed using a Quantum Design magnetic property measurement system MPMS®3 following standard procedures. Magnetic field sweeps were made in no-overshoot, persistent mode. The temperature sweeps were made at a rate of 5 K per minute. The estimated magnetic moments were determined from an average of two scans. For remanent magnetization measurements, the films were field-cooled from RT to 10 K with an external field of 2 T applied in-plane, and the superconducting magnet quenched before starting the temperature dependence.

XMCD

The XMCD measurements were performed on the DEIMOS beamline[45] of synchrotron SOLEIL. A XAS spectrum is obtained by continuously moving the energy of the monochromator over the energy range of interest while synchronizing the energy and polarization of the undulator to the energy of the monochromator[46]. The XMCD spectrum is obtained from four measurements, where both the circular helicity and the direction of the applied magnetic field are flipped.

Ab initio calculations

First-principle calculations were performed using the Vienna Ab-initio Simulation Package (VASP)[47,48], employing projector augmented wave (PAW)[49,50] for potentials with the plane wave energy cutoff in all the calculations set to 550 eV, and the generalized gradient approximation (GGA)[51] for the exchange-correlation energy. As a first step, ionic relaxation of Fe_5GeTe_2 bulk structure was performed with *k*-point grids of $7 \times 7 \times 1$ and 0.01 eV $Å^{-1}$ force tolerance during optimization of the atomic positions. The in-plane (out-of-plane) lattice parameter was fixed to 4.07 (29.3) Å. Next, a self-consistent calculation with $21 \times 21 \times 3$ *k*-point grids was realized to obtain the charge density wave and the atomic spin moments. Finally, the orbital moments were obtained by performing a non-self-consistent calculation with spin-orbit coupling included with the quantization axis set along [001].

DATA AVAILABILITY

All data needed to evaluate the conclusions in the paper are present in the paper and/or the Supplementary Materials. Additional data related to this paper may be requested from the authors.

Received: 21 June 2021; Accepted: 18 January 2022;
Published online: 23 February 2022

REFERENCES

1. Mermin, N. D. & Wagner, H. Absence of ferromagnetism or antiferromagnetism in one- or two-dimensional isotropic Heisenberg models. *Phys. Rev. Lett.* **17**, 1133–1136 (1966).
2. Gong, C. et al. Discovery of intrinsic ferromagnetism in two-dimensional van der Waals crystals. *Nature* **546**, 265–269 (2017).
3. Huang, B. et al. Layer-dependent ferromagnetism in a van der Waals crystal down to the monolayer limit. *Nature* **546**, 270–273 (2017).
4. Wang, X. et al. Raman spectroscopy of atomically thin two-dimensional magnetic iron phosphorus trisulfide (FePS3) crystals. *2D Mater.* **3**, 031009 (2016).
5. Fei, Z. et al. Two-dimensional itinerant ferromagnetism in atomically thin Fe3GeTe2. *Nat. Mater.* **17**, 778–782 (2018).
6. Seo, J. et al. Nearly room temperature ferromagnetism in a magnetic metal-rich van der Waals metal. *Sci. Adv.* **6**, eaay8912 (2020).
7. May, A. F. et al. Ferromagnetism near room temperature in the cleavable van der Waals crystal Fe5GeTe2. *ACS Nano* **13**, 4436–4442 (2019).
8. Kim, K. et al. Large anomalous Hall current induced by topological nodal lines in a ferromagnetic van der Waals semimetal. *Nat. Mater.* **17**, 794–799 (2018).
9. You, Y. et al. Angular dependence of the topological Hall effect in the uniaxial van der Waals ferromagnet Fe3GeTe2. *Phys. Rev. B* **100**, 134441 (2019).
10. Ding, B. et al. Observation of magnetic skyrmion bubbles in a van der Waals ferromagnet Fe3GeTe2. *Nano Lett.* **20**, 868–873 (2020).
11. Park, T.-E. et al. Neel-type skyrmions and their current-induced motion in van der Waals ferromagnet-based heterostructures. *Phys. Rev. B* **103**, 104410 (2021).
12. Zhang, Y. et al. Emergence of Kondo lattice behavior in a van der Waals itinerant ferromagnet, Fe3GeTe2. *Sci. Adv.* **4**, eaao6791 (2018).
13. Wang, Z. et al. Tunneling spin valves based on Fe3GeTe2/hBN/Fe3GeTe2 van der Waals heterostructures. *Nano Lett.* **18**, 4303–4308 (2018).
14. Freitas, D. C. et al. Ferromagnetism in layered metastable 1T-CrTe2. *J. Phys. Condens. Matter* **27**, 176002 (2015).
15. Zhang, X. et al. Room-temperature intrinsic ferromagnetism in epitaxial CrTe2 ultrathin films. *Nat. Commun.* **12**, 2492 (2021).
16. Deiseroth, H.-J., Aleksandrov, K., Reiner, C., Kienle, L. & Kremer, R. K. Fe3GeTe2 and Ni3GeTe2—two new layered transition-metal compounds: crystal structures, HRTEM investigations, and magnetic and electrical properties. *Eur. J. Inorg. Chem.* **2006**, 1561–1567 (2006).
17. Chen, B. et al. Magnetic properties of layered itinerant electron ferromagnet Fe3GeTe2. *J. Phys. Soc. Jpn.* **82**, 124711 (2013).
18. Deng, Y. et al. Gate-tunable room-temperature ferromagnetism in two-dimensional Fe3GeTe2. *Nature* **563**, 94–99 (2018).
19. Tian, C. et al. Tunable magnetic properties in van der Waals crystals (Fe1−xCox) 5GeTe2. *Appl. Phys. Lett.* **116**, 202402 (2020).
20. Yang, M. et al. Highly enhanced Curie temperature in Ga-implanted Fe3GeTe2 van der Waals material. *Adv. Quantum Technol.* **3**, 2000017 (2020).
21. Wang, H. et al. Above room-temperature ferromagnetism in Wafer-Scale two-dimensional van der Waals Fe3GeTe2 tailored by a topological insulator. *ACS Nano* **14**, 10045–10053 (2020).
22. Li, Q. et al. Patterning-induced ferromagnetism of Fe3GeTe2 van der Waals materials beyond room temperature. *Nano Lett.* **18**, 5974–5980 (2018).
23. May, A. F., Bridges, C. A. & McGuire, M. A. Physical properties and thermal stability of Fe5GeTe2 single crystals. *Phys. Rev. Mater.* **3**, 104401 (2019).
24. Joe, M., Yang, U. & Lee, C. First-principles study of ferromagnetic metal Fe5GeTe2. *Nano Mater. Sci.* **1**, 299–303 (2019).
25. Yamagami, K. et al. Itinerant ferromagnetism mediated by giant spin polarization of the metallic ligand band in the van der Waals magnet Fe5GeTe2. *Phys. Rev. B* **103**, L060403 (2021).
26. May, A. F., Du, M.-H., Cooper, V. R. & McGuire, M. A. Tuning magnetic order in the van der Waals metal Fe5GeTe2 by cobalt substitution. *Phys. Rev. Mater.* **4**, 074008 (2020).
27. Li, Z. et al. Magnetic critical behavior of the van der Waals Fe5GeTe2 crystal with near room temperature ferromagnetism. *Sci. Rep.* **10**, 15345 (2020).
28. Liu, S. et al. Wafer-scale two-dimensional ferromagnetic Fe 3 GeTe 2 thin films grown by molecular beam epitaxy. *npj 2D Mater. Appl.* **1**, 1–7 (2017).
29. Burch, K. S., Mandrus, D. & Park, J.-G. Magnetism in two-dimensional van der Waals materials. *Nature* **563**, 47–52 (2018).
30. Li, P. et al. Single-layer CrI3 grown by molecular beam epitaxy. *Sci. Bull.* **65**, 1064–1071 (2020).
31. Bedoya-Pinto, A. et al. Intrinsic 2D-XY ferromagnetism in a van der Waals monolayer. *Science* **374**, 616–620 (2021).
32. Li, B. et al. Van der Waals epitaxial growth of air-stable CrSe2 nanosheets with thickness-tunable magnetic order. *Nat. Mater.* https://doi.org/10.1038/s41563-021-00927-2 (2021).
33. Stahl, J., Shlaen, E. & Johrendt, D. The van der Waals ferromagnets Fe5−δGeTe2 and Fe5−δ−xNixGeTe2 – crystal structure, stacking faults, and magnetic properties. *Z. Anorg. Allg. Chem.* **644**, 1923–1929 (2018).
34. Renaud, G., Barbier, A. & Robach, O. Growth, structure, and morphology of the Pd/MgO(001) interface: Epitaxial site and interfacial distance. *Phys. Rev. B* **60**, 5872–5882 (1999).
35. Guillet, T. et al. Magnetotransport in Bi2Se3 thin films epitaxially grown on Ge (111). *AIP Adv.* **8**, 115125 (2018).
36. Chen, C. T. et al. Experimental confirmation of the X-ray magnetic circular dichroism sum rules for iron and cobalt. *Phys. Rev. Lett.* **75**, 152–155 (1995).
37. Stöhr, J. Exploring the microscopic origin of magnetic anisotropies with X-ray magnetic circular dichroism (XMCD) spectroscopy. *J. Magn. Magn. Mater.* **200**, 470–497 (1999).
38. Tan, C. et al. Gate-controlled magnetic phase transition in a van der Waals magnet Fe5GeTe2. *Nano Lett.* **21**, 5599–5605 (2021).
39. Ohta, T. et al. Enhancement of coercive field in atomically-thin quenched Fe5GeTe2. *Appl. Phys. Express* **13**, 043005 (2020).
40. Zhang, H. et al. Itinerant ferromagnetism in van der Waals Fe5GeTe2 crystals above room temperature. *Phys. Rev. B* **102**, 064417 (2020).
41. Zhao, B. et al. Van der Waals Magnet based Spin-Valve Devices at Room Temperature. Preprint at https://arxiv.org/abs/2107.00310 (2021).
42. Alahmed, L. et al. Magnetism and spin dynamics in room-temperature van der Waals magnet Fe5GeTe2. *2D Mater.* **8**, 045030 (2021).
43. Stadelmann, P. Image analysis and simulation software in transmission electron microscopy. *Microsc. Microanal.* **9**, 60–61 (2003).
44. Allen, L. J., D'Alfonso, A. J. & Findlay, S. D. Modelling the inelastic scattering of fast electrons. *Ultramicroscopy* **151**, 11–22 (2015).
45. Ohresser, P. et al. DEIMOS: A beamline dedicated to dichroism measurements in the 350–2500 eV energy range. *Rev. Sci. Instrum.* **85**, 013106 (2014).
46. Joly, L. et al. Fast continuous energy scan with dynamic coupling of the monochromator and undulator at the DEIMOS beamline. *J. Synchrotron Radiat.* **21**, 502–506 (2014).
47. Kresse, G. & Furthmüller, J. Efficiency of ab-initio total energy calculations for metals and semiconductors using a plane-wave basis set. *Comput. Mater. Sci.* **6**, 15–50 (1996).
48. Kresse, G. & Furthmüller, J. Efficient iterative schemes for ab initio total-energy calculations using a plane-wave basis set. *Phys. Rev. B* **54**, 11169–11186 (1996).
49. Blöchl, P. E. Projector augmented-wave method. *Phys. Rev. B* **50**, 17953–17979 (1994).
50. Kresse, G. & Joubert, D. From ultrasoft pseudopotentials to the projector augmented-wave method. *Phys. Rev. B* **59**, 1758–1775 (1999).

51. Perdew, J. P., Burke, K. & Ernzerhof, M. Generalized gradient approximation made simple. *Phys. Rev. Lett.* **77**, 3865–3868 (1996).
52. Momma, K. & Izumi, F. VESTA 3 for three-dimensional visualization of crystal, volumetric and morphology data. *J. Appl. Cryst.* **44**, 1272–1276 (2011).

ACKNOWLEDGEMENTS

The MBE reactors were funded by the project Minatec LABS 2018 N°2018 AURA P3 and the project EPI2D of the University Grenoble Alpes IDEX. We acknowledge the financial support from the UGA IDEX IRS/EVASPIN, the ANR projects ELMAX (ANR-20-CE24-0015) and MAGICVALLEY (ANR-18-CE24-0007), and the King Abdullah University of Science and Technology under grant number OSR-2018-CRG7-3717, the DARPA TEE program through Grant MIPR# HR0011831554 from the DOI, European Union's Horizon 2020 research and innovation Programme under grant agreement 881603 (Graphene Flagship), and the LANEF framework (ANR-10-LABX-51-01) for its support with mutualized infrastructure.

AUTHOR CONTRIBUTIONS

The sample preparation, growth, and the SQUID measurements were done by M.R., G. G., and F.B. XRD was performed by A.M. The AFM scans were made by G.G. The STEM cross-sections and simulations were done by H.O. and D.D. XMCD was done by F.B., G. G., D.L., and P.O. RBS was perform by C.V., J.-F.J., and D.J. A.H. and M.C. performed the ab initio simulations. The study was supervised by F.B., O.B., and M.J. M.R. and F.B. wrote the paper, and all authors contributed to the discussion of the results.

COMPETING INTERESTS

The authors declare no competing interests.

ADDITIONAL INFORMATION

Supplementary information The online version contains supplementary material available at https://doi.org/10.1038/s41699-022-00285-w.

Correspondence and requests for materials should be addressed to Mário Ribeiro or Frédéric Bonell.